

See discussions, stats, and author profiles for this publication at: <https://www.researchgate.net/publication/268155430>

Facile Fabrication of Carbon Ultramicro- to Nanoelectrode Arrays with Tunable Voltammetric Response

ARTICLE *in* ANALYTICAL CHEMISTRY · NOVEMBER 2014

Impact Factor: 5.64 · DOI: 10.1021/ac503296x · Source: PubMed

CITATIONS

2

READS

33

3 AUTHORS, INCLUDING:



Jacob Goran

Instrumentation Laboratory, Bedford, United ...

23 PUBLICATIONS 111 CITATIONS

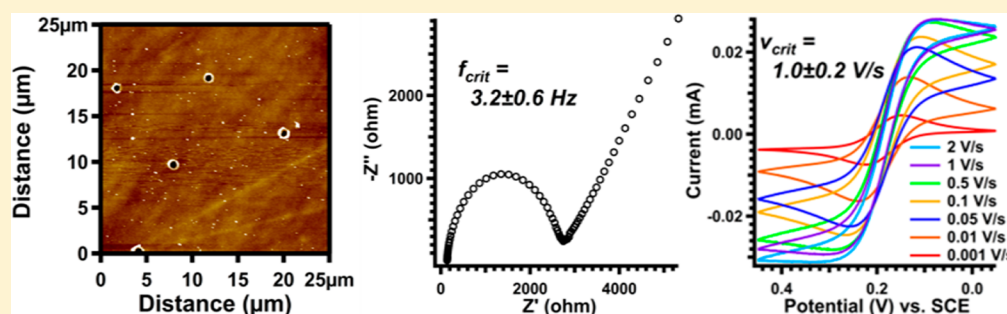
SEE PROFILE

Facile Fabrication of Carbon Ultramicro- to Nanoelectrode Arrays with Tunable Voltammetric Response

Jonathon Duay, Jacob M. Goran, and Keith J. Stevenson*

Department of Chemistry, Center for Nano- and Molecular Science and Technology, The University of Texas at Austin, Austin, Texas 78712, United States

S Supporting Information



ABSTRACT: The voltammetric response for nano- to micrometer-sized electrode arrays are represented by two major regimes: a sigmoidal shaped $i-v$ response for arrays acting as individual electrodes in parallel and peak-shaped $i-v$ response for arrays acting as an ensemble in concert. Here, we present a facile and versatile technique to fabricate ultramicro- to nanoelectrode arrays using atomic layer deposition of insulating Al_2O_3 on conductive carbon films masked by 1.54, 11, or 90- μm -diameter polystyrene spheres (PSS). The ratio between the interelectrode distance and the electrode radii of the electrode arrays is a predictable function of the PSS radius used in fabrication, resulting in electrode arrays with a tunable voltammetric response. Arrays are characterized utilizing cyclic voltammetry and electrochemical impedance spectroscopy, which provides the critical scan rate, ν_{crit} , the scan rate at which the radial diffusion layers of the individual electrodes overlap and appear as a single linear diffusion layer. Thus, below ν_{crit} , the electrode has a peak-shaped $i-v$ response associated with semi-infinite linear diffusion, whereas above this critical scan rate, the $i-v$ response is sigmoidal as a result of hemispherical radial diffusion. Results indicate that the critical scan rates are 6.6, 1.0, and 0.01 V/s for the 1.54, 11, and 90 μm PSS prepared electrode arrays, respectively.

Micro- and nano- electrodes are well-known for their high signal-to-noise ratio due to radial diffusion profiles associated with fast steady state diffusion and low background/capacitive current.^{1,2} Although these electrodes can exhibit a large current density, their absolute current signal is quite small (nanoamp to picoamp range), indicative of their electrode area.³ To overcome this disadvantage, arrays of microelectrodes, where the current increases proportionally to the number of electrodes in the array, are receiving significant attention.^{2,4–9} Microelectrode arrays have been applied to trace analysis in environmental monitoring and biological sensors and as detectors for electrophoresis among other applications.^{3,6,10–19}

The voltammetric response for microelectrode arrays in conjunction with an appropriate redox-active species is directly affected by the ratio between the average interelectrode distance, d , and the average microelectrode radius, a , as well as the scan rate, ν .^{3,6,9,20} Assuming an identical scan rate, larger d/a ratios result in voltammetric responses characteristic of individual microelectrodes whereas smaller d/a ratios display macroelectrode behavior. Although microelectrode behavior is ideal for maximum current density and enhanced kinetic response, macroelectrode behavior is advantageous in gen-

erator-collector mode or as individually addressable microelectrode arrays in which sets of electrodes are held at different potentials in the same diffusion layer.^{21–24} Therefore, it is important to have a facile fabrication technique that can produce a wide range of d/a ratios for a desired application.

Although reports on the synthesis of microelectrode and ultramicroelectrode arrays in the literature are prevalent, almost all of the fabrication methods for these arrays are quite lengthy and cumbersome, requiring demanding processing steps (i.e., microtransfer molding,¹¹ photolithography,^{9,23,25} chemical mechanical polishing,^{9,26} cyanide etching of self-assembled monolayers,⁴ e-beam lithography,⁷ and chemical vapor deposition^{7,9,21,26–30}), expensive equipment, and precise instrumentation. These demands often result in limited tunability of the electrode array material and dimensions.

Here, we present a facile fabrication method that produces carbon electrode arrays over a wide d/a range. Commercially available polystyrene spheres (PSSs) with manufacturer stated

Received: August 23, 2014

Accepted: November 8, 2014

Published: November 8, 2014

diameters of 1.54, 11, or 90 μm are drop-cast on a conductive carbon pyrolyzed photoresist film (PPF) electrode, forming a hexagonal close-packed, two-dimensional, ordered network. These PSS arrays are then coated with Al_2O_3 using a commonly applied atomic layer deposition (ALD) procedure. The spheres are then removed, leaving behind carbon ultramicro- to nanoelectrodes (depending on the size of the sphere) where the PSS was in contact with the carbon film.

Electrochemical impedance spectroscopy (EIS) was used to obtain the critical scan rate, ν_{crit} , where the electrode array transitioned from individual electrodes operating in parallel to a “macro” linear-based diffusion regime. EIS was used initially to identify the critical frequency, f_{crit} , for the transition between the two diffusional regimes. The potential difference at this frequency was measured as the onset of the redox current to the arrival of the limiting current (ΔE , of 0.3 V) and finally multiplying ΔE by f_{crit} to determine the critical scan rate, ν_{crit} .

EXPERIMENTAL SECTION

Fabrication of Carbon Ultramicroelectrode Arrays (CUAs). Pyrolyzed photoresist films (PPFs) were prepared by a previously reported procedure, details of which can be found in the Supporting Information.^{31–33} Polystyrene spheres of 1.54, 11, or 90 μm diameters were drop-cast from a 10 wt % methanol suspension onto the PPF electrodes. After methanol evaporation, the electrodes were put on a hot plate held at 110 $^{\circ}\text{C}$ for 10 min to allow the PSSs to settle, promoting evenly size-distributed contact areas. Before atomic layer deposition (ALD), portions of the electrodes were masked using commercially available nail polish (Sally Hansen Insta-Dri) to allow connection to the circuit later. A Cambridge Nanotech Savannah S100 ALD system was then used to coat the electrodes with Al_2O_3 . The ALD recipe can be found in the Supporting Information. The ALD-coated hexagonally close-packed PSS film electrodes were then sonicated in methanol to physically remove the PSSs, followed by sonication in acetone to remove the nail polish, which also conveniently dissolves any PSSs that remained after the initial sonication. The electrodes are then successively sonicated in isopropyl alcohol and water. Finally, the electrodes are dried using a nitrogen stream prior to atomic force microscopy and electrochemical characterization.

Characterization of CUAs. The topography of the ultramicroelectrode arrays was measured by atomic force microscopy (AFM) performed using an Asylum Research MFP-3D instrument. Electrochemical measurements were performed using an AutoLab PGSTAT instrument.

RESULTS

The fabricated electrode arrays were characterized by AFM. The three arrays used here are henceforth labeled as 1.54CUA, 11CUA, and 90CUA corresponding to the 1.54-, 11-, and 90- μm -diameter spheres, respectively. Figure 1a–c, shows AFM micrographs obtained from the three different electrode arrays ($25 \times 25 \mu\text{m}$ scan area), and parts d–f of the figure show representative cross-sectional line scans across individual electrodes in each array (the particular electrode analyzed is circled in red). The electrodes are recessed $\sim 10 \text{ nm}$ below the ALD surface, indicating that the recession depth is controlled by the thickness of the ALD Al_2O_3 coating. Near the edge of each electrode, the alumina layer thickness increases by 5–15 nm, resulting in an annular ring around each electrode. This ring is explained by the conformal deposition of alumina on the

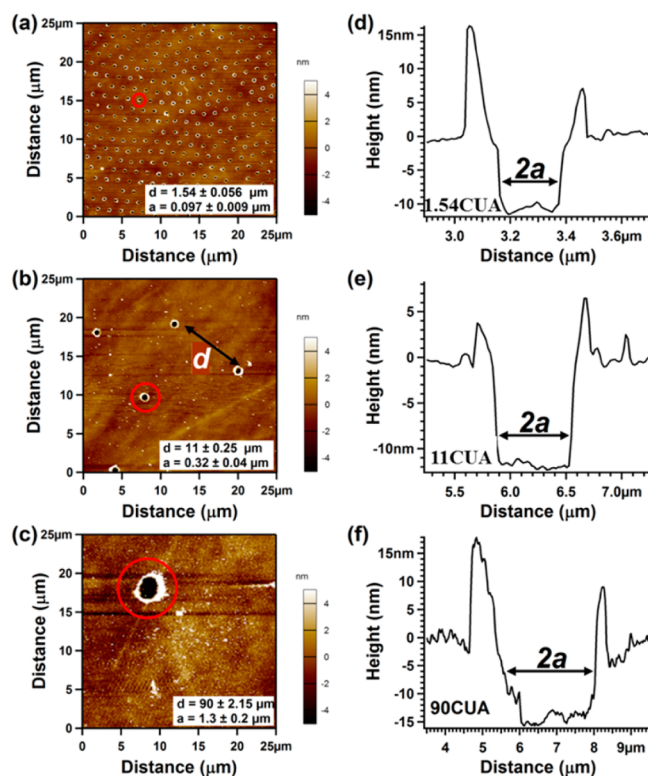
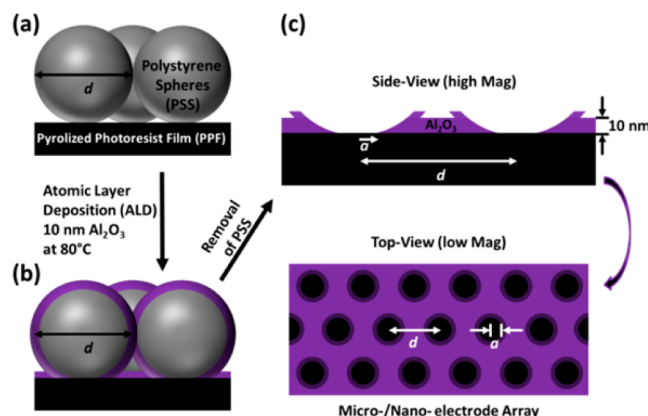


Figure 1. Atomic force microscopy (AFM) images of (a) 1.54CUA, (b) 11CUA, and (c) 90CUA carbon ultramicroelectrode arrays using a $25 \times 25 \mu\text{m}$ scan window. Cross-sectional linescans for electrodes circled in red in the AFM image directly to the left for the (d) 1.54CUA, (b) 11CUA, and (c) 90CUA.

PSSs during the ALD process, some of which remains after the sphere has been removed, illustrated in Scheme 1c below. Although these electrodes can be referred to as recessed, it was found that the electrochemical behavior closely resembles coplanar electrodes because this recession is insignificant compared with the radius of the electrode used here ($<10\%$ for the smallest 1.54CUA).^{4,6}

Scheme 1. Fabrication Process for the Carbon Electrode Arrays^a



^a(a) Polystyrene spheres (PSS) drop-cast on pyrolyzed photoresist. (b) PSS coated with 10 nm Al_2O_3 using atomic layer deposition. (c) Side-view and top-view illustrations of carbon microelectrode arrays after PSS removal by sonication and chemical dissolution.

Table 1. Dimensions of Carbon UME Arrays along with Their EIS-Derived Critical Frequency and Scan Rate

carbon UME array	diameter of PSS used, d (μm) ^a	radius of UME, a (μm)	d/a (unit less)	critical frequency, f_{crit} (s^{-1})	critical scan rate, ν_{crit} (V s^{-1})
1.54CUA	1.54 ± 0.056	0.097 ± 0.009	16 ± 2	22 ± 3	6.6 ± 0.9
11CUA	11 ± 0.25	0.32 ± 0.04	34 ± 5	3.2 ± 0.6	1.0 ± 0.2
90CUA	90 ± 2.15	1.3 ± 0.2	70 ± 10	0.03 ± 0.01	0.01 ± 0.004

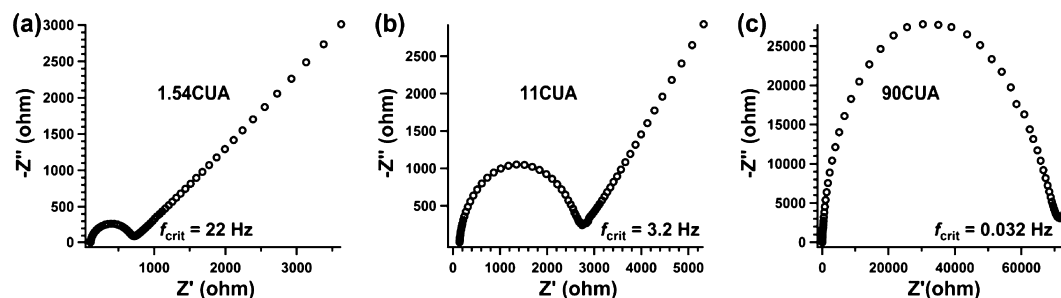
^aStatistics from Manufacturer.

Figure 2. Nyquist plots for the (a) 1.54CUA, (b) 11CUA, and (c) 90CUA UME arrays.

The average interelectrode distance, d , is dictated by the diameter of the PSS and is included in Figure 1a–c and Table 1. The average radius of the electrodes, a , was calculated from the line scans across the individual electrodes, as seen in Figure 1d–f. For the electrode arrays 1.54CUA, 11CUA, and 90CUA, average electrode radii of 0.097, 0.32, and 1.3 μm , were obtained, respectively.

The critical contact radius, a , which governs the size of the electrodes, is directed by the Johnson–Kendall–Roberts (JKR) model for elastic contact of a sphere on a substrate at zero applied load. The relationship $a \propto R^{2/3}$ (R = radius of sphere) can be inferred from the JKR model (see Supporting Information).³⁴ Therefore, d/a is subsequently proportional to $R^{1/3}$.

For the three electrode arrays fabricated here, 1.54CUA, 11CUA, and 90CUA, d/a values of 16, 34, and 70, respectively, were obtained. A plot of d/a versus $R^{1/3}$ for the three electrode arrays is displayed in Supporting Information Figure S1, revealing the expected linear trend with an R^2 value of 0.9994. The linear trend reiterates the d/a value, and thus, the voltammetric response of electrode arrays utilizing this method can be fine-tuned by choosing the appropriate size of PSS (commercially available with diameters between 0.05 and 90 μm).

In addition to the d/a ratio, the scan rate, ν , used during cyclic voltammetry (CV) also dictates whether the electrodes behave as UMEs in parallel or in concert. For instance, at faster scan rates, there is less time for the diffusion layer to advance and, thus, less chance for diffusion layers between adjacent electrodes to overlap. To describe this transition point, previous groups have used a series of cyclic voltammetry scan rates for which a 5% (or less) difference in the peak current from limiting current was chosen to be indicative of the electrode array operating as UMEs in parallel.^{6,35}

To objectively characterize the transition point between the macro- and microbehavior for each electrode array, electrochemical impedance spectroscopy (EIS) was employed. Previously, it has been shown that the EIS response (Nyquist plot) of electrode arrays consist of a semicircle at high frequencies and transition to a straight line at low frequencies.⁹ The semicircle region is generally characteristic of a kinetically controlled process, whereas the straight line region, also known

as the Warburg line, is characteristic of a diffusion-limited process. In this case, the frequency at which the EIS response changes from a semicircle to a straight line is analogous to the transition between the microelectrode behavior, in which each electrode behaves individually, to the macroelectrode behavior, in which diffusion layers overlap. The frequency of this transition is defined as the critical frequency, f_{crit} .

The Nyquist plots for the three arrays fabricated here are found in Figure 2a–c. All three plots contain a clearly defined semicircle and Warburg line. Note that the diameter of the semicircle, which is directly related to the charge transfer resistance, R_{ct} , increases concurrently with the size of the PSS used to fabricate the array. R_{ct} is inversely proportional to the electrode area. Additionally, the outer sphere redox probe employed here, ferrocenemethanol, displays an extremely facile electron transfer, observed in the EIS spectra of the nonpatterend, bare PPF electrodes as a Warburg line at every measured frequency (shown in the Supporting Information Figure S2). It is well-known that increasing radial diffusion by decreasing the electrode size allows the upper detection limit of fast electron transfers to be extended,³⁶ and k^0 for ferrocenemethanol has been measured at ~ 1 and 7 cm/s at nanoscale CNT³⁷ and Pt electrodes,^{36,38} respectively (at the limit for measuring k^0 by EIS).³⁹ As such, the R_{ct} observed in the EIS spectra is not actually the kinetics of electron transfer, since the transfer is too fast to be measured using this technique, but rather, a consequence of the decreasing overall electroactive surface area and increasing individual electrode diameter (and coordinating d/a relationship, concomitant with the PSS diameter).

The critical frequency, f_{crit} , where the semicircle and Warburg line meet, is observed to be 22, 3.2, and 0.03 Hz for the 1.54CUA, 11CUA, and 90CUA, respectively. A reciprocal of this frequency can be thought of as the time required to transition from a radial diffusion-controlled regime to a semi-infinite linear-diffusion controlled regime. Therefore, this time frame should also correlate to a critical scan rate where this transition can also be observed. The critical scan rate, ν_{crit} , can be assessed from the following equation:

$$\nu_{\text{crit}} = \Delta E f_{\text{crit}} \quad (1)$$

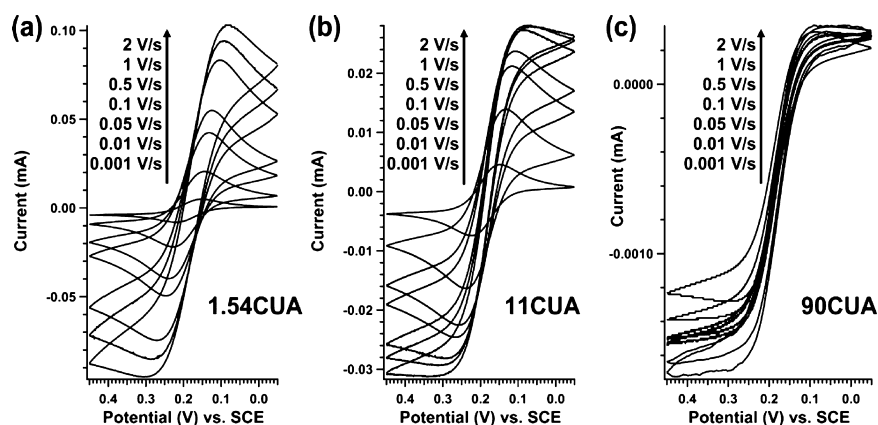


Figure 3. Cyclic voltammetry of the (a) 1.54-, (b) 11-, and (c) 90- μm -diameter PSS0-prepared carbon ultramicroelectrode arrays at scan rates between 0.001 and 2 V/s using 1 mM ferrocenemethanol in 0.1 M KCl and 0.1 M sodium phosphate buffer.

Here, the critical frequency is multiplied by the potential difference between the onset of the redox reaction and where the limiting current is attained, ΔE . A ΔE value of 0.3 V is employed here; however, we note that this value is somewhat arbitrary and depends heavily on the electrochemical kinetics. Nonetheless, for the reversible, kinetically fast redox probe used here, this value is appropriate and can be utilized to compare with other reports in the literature.²⁰

The critical scan rates for the 1.54CUA, 11CUA, and 90CUA electrode arrays can be found in Table 1. Any scan rate above these values should show microelectrode behavior, and any scan rate below these values should show intermediate to macroelectrode behavior.

To analyze the effectiveness of obtaining ν_{crit} through EIS, CV was performed on all three electrode arrays at scan rates between 0.001 and 2 V/s, shown in Figure 3. On the basis of the EIS information, we expect that at scan rates above ν_{crit} the i - ν curve should display a sigmoidal shape, and the limiting current should be independent of scan rate.

For the 1.54CUA, the CVs shift from the macroelectrode semi-infinite linear diffusion regime at low scan rates, with a CV identical to that of a PPF macroelectrode without any Al_2O_3 coating at 0.001 V/s (even though the exposed electroactive area is only 1.7% of the PPF macroelectrode), displayed in Supporting Information Figure S3a along with the background double layer current in Supporting Information Figure S3b, to an intermediate regime that begins to resemble a sigmoidal shape at the high scan rates. Higher scan rates, between 2 and 15 V/s found in Supporting Information Figure S3c, indicate that the limiting current becomes constant at between 6 and 10 V/s. This result is expected because the critical scan rate for this CUA was estimated at 6.6 V/s.

For the 11CUA, the voltammograms shift from an intermediate regime to the sigmoidal behavior with a transition between 0.5 and 2 V/s. Again, this is close to the predicted critical scan rate of 1.0 V/s for this electrode array. Finally, for the 90CUA, the i - ν response is sigmoidal for all but the very slowest scan rate (0.001 V/s), as estimated by the EIS analysis (predicted critical scan rate at 0.01 V/s). It should be noted that the steady state behavior is offset from the 0 x -axis because the voltammograms presented here are not the first scan from a fresh solution. In addition, it was determined that an insignificant amount of current can be attributed to pinholes and other defects in the Al_2O_3 layer from analysis of the i - ν

response of a completely ALD-coated PPF (see Supporting Information Figure S4).

Overall, the EIS determined ν_{crit} had excellent agreement with the experimentally observed transition through CV analysis. Currently, we are trying to understand how the critical scan rate relates to the electrochemical response since a power law decay is observed for the critical scan rate as a function of the PSS radius. For instance, it is found that a 60-times increase in the center-to-center distance (90CUA versus 1.54CUA) results in an almost 700-times decrease in the critical scan rate. Nonetheless, EIS is a simple and intuitive way to characterize the transition between an ultramicroelectrode array operating in parallel or in concert.

CONCLUSION

Carbon ultramicroelectrode (UME) arrays were fabricated utilizing a simple synthesis technique that permits precise control over the ratio between the interelectrode UME distance, d , and the radius of the individual UMES, a . AFM was used to characterize the CUA topology and analyze how this d/a ratio for these electrodes changes as a function of PSS diameter. EIS results for the three CUAs allowed unambiguous determination of the critical scan rate, ν_{crit} , the scan rate at which the CUA operates as a collection of individual UMES working in parallel rather than an ensemble of UMES working in concert. Cyclic voltammetry was used to verify the critical scan rate obtained from EIS, displaying excellent agreement. The ν_{crit} was calculated to be 6.6, 1.0, and 0.01 V/s for the 1.54CUA, 11CUA, and 90CUA electrode arrays, respectively. This fabrication technique allows for the selection of a specific cyclic voltammogram response by simply choosing the radius of PSS used to fabricate the electrode array, given an appropriate scan rate. Moreover, the underlying carbon film produced by pyrolyzing a photoresist could potentially be photopatterned to allow production of individually addressable electrode. Finally, although photoresist-derived carbon is used for this fabrication example, this fabrication process can be easily adapted and applied to make electrode arrays on other conductive substrates, such as gold and platinum, thus creating a versatile experimental platform that can be easily tailored to the electrochemical detection method that is desired.

■ ASSOCIATED CONTENT

■ Supporting Information

Detailed experimental protocols, JKR contact mechanics. Figure S1: plot of d/a versus cube root of PSS radius. Figure S2: EIS spectra of PPF macroelectrode. Figure S3: comparison of signal and background voltammograms for the 1.54CUA array and a PPF carbon macroelectrode, and voltammograms of the 1.54CUA array between 2 and 15 V/s scan rates. Figure S4: $i-v$ curve of completely ALD Al_2O_3 coated PPF. This material is available free of charge via the Internet at <http://pubs.acs.org>

■ AUTHOR INFORMATION

Corresponding Author

*E-mail: stevenson@mail.utexas.edu.

Author Contributions

The manuscript was written through contributions of all authors. All authors have given approval to the final version of the manuscript.

Notes

The authors declare no competing financial interest.

■ ACKNOWLEDGMENTS

J.D. acknowledges support from the program "Understanding Charge Separation and Transfer at Interfaces in Energy Materials (EFRC:CST)," an Energy Frontier Research Center funded by the U.S. Department of Energy, Office of Science, Office of Basic Energy Sciences, under Award Number DE-SC0001091. K.J.S. and J.M.G. acknowledge financial support of this work was provided by the R.A. Welch Foundation (Grant F-1529).

■ REFERENCES

- (1) Achterberg, E. P. *Trends Anal. Chem.* **1996**, *15*, 550.
- (2) Chen, R.; Li, Y.; Huo, K.; Chu, P. K. *RSC Adv.* **2013**, *3*, 18698–18715.
- (3) Hood, S. J.; Kampouris, D. K.; Kadara, R. O.; Jenkinson, N.; del Campo, F. J.; Muñoz, F. X.; Banks, C. E. *Analyst* **2009**, *134*, 2301–2305.
- (4) Baker, W. S.; Crooks, R. M. *J. Phys. Chem. B* **1998**, *102*, 10041–10046.
- (5) Compton, R. G.; Wildgoose, G. G.; Rees, N. V.; Streeter, I.; Baron, R. *Chem. Phys. Lett.* **2008**, *459*, 1–17.
- (6) Guo, J.; Lindner, E. *Anal. Chem.* **2009**, *81*, 130–138.
- (7) Hees, J.; Hoffmann, R.; Kriele, A.; Smirnov, W.; Obloh, H.; Glorier, K.; Raynor, B.; Driad, R.; Yang, N.; Williams, O. a; Nebel, C. E. *ACS Nano* **2011**, *5*, 3339–3346.
- (8) Koehne, J. E.; Marsh, M.; Boakye, A.; Douglas, B.; Kim, I. Y.; Chang, S.-Y.; Jang, D.-P.; Bennet, K. E.; Kimble, C.; Andrews, R.; Meyyappan, M.; Lee, K. H. *Analyst* **2011**, *136*, 1802–1805.
- (9) Siddiqui, S.; Arumugam, P. U.; Chen, H.; Li, J.; Meyyappan, M. *ACS Nano* **2010**, *4*, 955–961.
- (10) Ordeig, O.; Banks, C. E.; Del Campo, J.; Munoz, F. X.; Compton, R. G. *Electroanalysis* **2006**, *18*, 573–578.
- (11) Li, F.; Xue, M.; Ma, X.; Zhang, M.; Cao, T. *Anal. Chem.* **2011**, *83*, 6426–6430.
- (12) Berduque, A.; Lanyon, Y. H.; Beni, V.; Herzog, G.; Watson, Y. E.; Rodgers, K.; Stam, F.; Alderman, J.; Arrigan, D. W. M. *Talanta* **2007**, *71*, 1022–1030.
- (13) Del Campo, F. J.; Ordeig, O.; Vignes, N.; Godino, N.; Mas, J.; Munoz, F. X. *Sens. Actuators, B* **2007**, *126*, 515–521.
- (14) Nebling, E.; Grunwald, T.; Albers, J.; Schaefer, P.; Hintsche, R. *Anal. Chem.* **2004**, *76*, 689–696.
- (15) Wassum, K. M.; Tolosa, V. M.; Wang, J.; Walker, E.; Monbouquette, H. G.; Maidment, N. T. *Sensors* **2008**, *8*, 5023–5036.
- (16) Chen, Y.; Guo, C.; Lim, L.; Cheong, S.; Zhang, Q.; Tang, K.; Reboud, J. *Anal. Chem.* **2008**, *80*, 1133–1140.
- (17) Feeney, R.; Kounaves, S. P. *Electroanalysis* **2000**, *12*, 677–684.
- (18) Albers, J.; Grunwald, T.; Nebling, E.; Piechotta, G.; Hintsche, R. *Anal. Bioanal. Chem.* **2003**, *377*, 521–527.
- (19) Liu, J.; Zhou, W.; You, T.; Li, F.; Wang, E.; Dong, S. *Anal. Chem.* **1996**, *68*, 3350–3353.
- (20) Davies, T. J.; Compton, R. G. *J. Electroanal. Chem.* **2005**, *585*, 63–82.
- (21) Tomčík, P. *Sensors (Basel)* **2013**, *13*, 13659–13684.
- (22) Ugo, P.; Moretto, L. M.; Vezzà, F. *ChemPhysChem* **2002**, *3*, 917–925.
- (23) Zhu, F.; Yan, J.; Lu, M.; Zhou, Y.; Yang, Y.; Mao, B. *Electrochim. Acta* **2011**, *56*, 8101–8107.
- (24) Han, D.; Kim, Y. R.; Kang, C. M.; Chung, T. D. *Anal. Chem.* **2014**, *86*, 5991–5998.
- (25) Ordeig, O.; Banks, C. E.; del Campo, F. J.; Muñoz, F. X.; Davis, J.; Compton, R. G. *Electroanalysis* **2006**, *18*, 247–252.
- (26) Li, J.; Koehne, J.; Cassell, A.; Chen, H.; Ng, H.; Ye, Q.; Fan, W.; Han, J.; Meyyappan, M. *Electroanalysis* **2005**, *17*, 15–27.
- (27) Hees, J.; Hoffmann, R.; Yang, N.; Nebel, C. E. *Chemistry* **2013**, *19*, 11287–11292.
- (28) Sun, G.; Huang, Y.; Zheng, L.; Zhan, Z.; Zhang, Y.; Pang, J. H. L.; Wu, T.; Chen, P. *Nanoscale* **2011**, *3*, 4854–4858.
- (29) Tu, Y.; Lin, Y.; Yantasee, W.; Ren, Z. *Electroanalysis* **2005**, *17*, 79–84.
- (30) Swisher, L. Z.; Syed, L. U.; Prior, A. M.; Madiyar, F. R.; Carlson, K. R.; Nguyen, T. A.; Hua, D. H.; Li, J. *J. Phys. Chem. C* **2013**, *117*, 4268–4277.
- (31) Walker, E. K.; Vanden Bout, D. A.; Stevenson, K. J. *J. Phys. Chem. C* **2011**, *115*, 2470–2475.
- (32) Donner, S.; Li, H. W.; Yeung, E. S.; Porter, M. D. *Anal. Chem.* **2006**, *78*, 2816–2822.
- (33) Tian, H.; Bergren, A. J.; McCreery, R. L. *Appl. Spectrosc.* **2007**, *61*, 1246–1253.
- (34) Johnson, K. L.; Kendall, K.; Roberts, A. D. *Proc. R. Soc. A* **1971**, *324*, 301–313.
- (35) Amatore, C.; Savéant, J. M.; Tessier, D. *J. Electroanal. Chem. Interfacial Electrochem.* **1983**, *147*, 39–51.
- (36) Sun, P.; Mirkin, M. V. *Anal. Chem.* **2006**, *78*, 6526–6534.
- (37) Patil, A. V.; Beker, A. F.; Wiertz, F. G. M.; Heering, H. A.; Coslovich, G.; Vlijm, R.; Oosterkamp, T. H. *Nanoscale* **2010**, *2*, 734–738.
- (38) Li, Y.; Bergman, D.; Zhang, B. *Anal. Chem.* **2009**, *81*, 5496–5502.
- (39) Bard, A. J.; Faulkner, L. R. *Electrochem. Methods: Fundam. Appl.* **2001**, *677*, 335–348.